

Predictive modeling of post bioprinting structure formation

Cite this: *Soft Matter*, 2014, 10, 1790Matthew McCune,^{†a} Ashkan Shafiee,^{†a} Gabor Forgacs^{abc} and Ioan Kosztin^{*a}

Cellular particle dynamics (CPD) is an effective computational method to describe the shape evolution and biomechanical relaxation processes in systems composed of micro tissues such as multicellular aggregates. Therefore, CPD is a useful tool to predict the outcome of postprinting structure formation in bioprinting. The predictive power of CPD has been demonstrated for multicellular systems composed of identical volume-conserving spherical and cylindrical bioink units. Experiments and computer simulations were related through an independently developed theoretical formalism based on continuum mechanics. Here we generalize the CPD formalism to (i) include non-identical bioink particles often used in specific bioprinting applications, (ii) describe the more realistic experimental situation in which during the post-printing structure formation *via* the fusion of spherical bioink units the volume of the system decreases, and (iii) directly connect CPD simulations to the corresponding experiments without the need of the intermediate continuum theory inherently based on simplifying assumptions.

Received 6th November 2013
Accepted 20th January 2014

DOI: 10.1039/c3sm52806e

www.rsc.org/softmatter

1. Introduction

Bioprinting has recently emerged as a powerful method to fabricate complex biological structures such as tissues and organs.¹ Several specific technologies have been developed which all share the following common features.^{1,2} Bioink units are delivered by special purpose printers into a convenient supporting environment. The biological structures form post-printing by the organization of the discrete bioink units into the continuous biological structure. The specific technologies differ in the nature and composition of the bioink and the method of their delivery. The bioink units vary from drops of culture medium or hydrogel containing a single to a few cells,^{3,4} to micro tissues composed of only cells^{5,6} or cell-laden hydrogels.^{7,8} Depending on the bioink the delivery method can utilize an inkjet printer,⁹ laser guidance,^{10,11} acoustic actuation,¹² micro valve dispensers⁴ or extrusion.⁵

Another common feature of the various bioprinting approaches is that postprinting structure formation is largely uncontrolled. In our technology, in which the discrete bioink units are multicellular spherical or cylindrical microtissues,^{13,14} their organization upon delivery takes place through processes known to act in embryonic morphogenesis, such as tissue fusion and cell sorting.⁶ However, no guiding principles exist to determine in advance when the developing tissue or organ structure

is ready for use (*e.g.*, implantation), thus this task is time consuming, expensive and is largely based on trial and error.

To address the lack of predictability concerning postprinting structure formation, at least in the technology utilizing micro-tissues as bioink, we have developed a computational method, referred to as *cellular particle dynamics* (CPD),^{15–17} that can predict quantitatively the time evolution of the shape of multicellular systems during biomechanical relaxation processes, *e.g.*, the fusion of the discrete bioink particles. Besides CPD, there exist several cell-based theoretical models and computational methods for describing various features of the dynamics of multicellular systems. For example, to model gastrulation, Odell and coworkers represented the cell as a collection of coupled viscoelastic elements.¹⁸ To describe cell sorting, Glazier and Graner built a cell using the Cellular Potts Model (*i.e.*, a collection of contiguous spins on a discrete lattice).^{19,20} Palsson and Othmer considered cells as deformable viscoelastic ellipsoids and studied how the motion of individual cells leads to the collective motion of an aggregate of cells.²¹ To model blastula formation, Drasdo and Forgacs performed Monte Carlo simulations based on a multi-scale model and first principle equations of motion.²² For modeling the forces and the resulting dynamics in 3D multicellular systems, Brodland and coworkers introduced a cell-level finite element method.^{23–25} To describe the shape evolution of multicellular systems during post-bioprinting structure formation, as well as cell sorting, a method based on Kinetic Monte Carlo simulations was introduced by Flenner *et al.*¹⁶ and then further developed and extended by Sun and Wang.²⁶ Finally, Newman's powerful and versatile *subcellular element method* (ScEM)²⁷ can be used to study a variety of multicellular processes, *e.g.*, cell division, adaptive cellular

^aDepartment of Physics and Astronomy, University of Missouri, Columbia, MO 65211, USA. E-mail: kosztini@missouri.edu

^bDepartment of Biological Sciences, University of Missouri, Columbia, MO 65211, USA

^cDepartment of Biomedical Engineering, University of Missouri, Columbia, MO 65211, USA

[†] These authors contributed equally to this work.

shape deformations and primitive streak formation.^{28–31} While conceptually CPD and ScEM are similar, the difference between them is manifest in (i) the properties and parametrization of the employed force field, and (ii) the scope of their applications.

In CPD cells are modeled as a set of *cellular particles* (CPs) that interact *via* short-range contact interactions. The time evolution of the spatial conformation of the multicellular system is determined by following the trajectories of all cellular particles through integration of their equations of motion. The CPD model parameters are determined by matching the shape evolution of the simulated system with that of the experimental system. Furthermore, the connection between the CPD and experimental time units is established by applying a theoretical continuum model suitable to describe quantitatively the same multicellular fusion process (e.g., fusion of two spherical aggregates) studied both experimentally and through CPD simulation. Once this connection is established, CPD simulations can be used to quantitatively predict the shape evolution of any multicellular system (in particular the one composed of the discrete bioink units in the construction of a vascular graft¹⁵) built of the same cell type used in the experiments to determine the CPD parameters.

We have demonstrated the predictive power of the CPD simulations for multicellular systems composed of identical spherical^{15–17} and cylindrical¹⁵ bioink units. However, bio-printed structures are often built of nonidentical units, such as spherical aggregates of differing diameters. In addition, the CPD formalism in its current form applies only to volume conserving multicellular systems, which experimentally is seldom the case. If the characteristic fusion time of the bioink units is longer than the cell cycle time of the composing cells, the volume of the system grows during structure formation. If the bioink units are loose, upon their fusion, the volume of the system may decrease.

In the present work we expand on the CPD formalism to make it applicable to more general bioprinting schemes. In particular we discuss the fusion of unequal size bioink units, by developing the continuum theory for this case and testing it by comparing experiments with CPD simulations. Furthermore, we extend the continuum theory for non volume conserving fusion processes, and demonstrate that in fact CPD simulations can be used to describe and predict the shape evolution of multicellular systems whose volume changes in time. Finally, we show how CPD can be employed to directly predict the shape evolution of multicellular systems without the need to employ the intermediate continuum theory, which unavoidably is valid only under well defined conditions not always fulfilled by the evolving bioprinted structure.

2. Fusion of two uneven spherical aggregates

2.1. Theory

Soft-tissue aggregates behave as highly viscous complex liquids.³² When two spherical cell aggregates are brought into contact, they will fuse into a final spheroidal structure³³ (the

configuration with the lowest surface energy for given volume). The fusion process is driven by surface tension forces and is resisted by the internal viscosity of the system. It has been observed experimentally that at any time during the fusion of two initially spherical aggregates the shape of the system is that of two contiguous spherical caps.³³ This geometrical simplicity permits the analytical description of the dynamics of the fusion process by employing only energy and mass conservation. Such an approach, originally proposed by Frenkel³⁴ and Eshelby³⁵ for the sintering of highly viscous molten drops, has been successfully applied to describe the fusion of even (identical) spherical (and also cylindrical) aggregates.¹⁵ Here we extend the theory to the fusion of uneven (non-identical) spherical aggregates. First, we assume that the volume of the system remains constant during the fusion process. Later, we generalize our results for the case when fusion is accompanied by volume change as observed in most experiments.

The fusing uneven aggregates are modeled as two spherical caps of radii $R_1(\theta_1) > R_2(\theta_2)$, with a circular contact (“neck”) region of radius

$$r = R_1 \sin \theta_1 = R_2 \sin \theta_2 \quad (1)$$

where the fusion angles $\theta_{1,2}$ are defined in Fig. 1. The initial radii of the uneven aggregates are $R_{i0} = R_i(0)$, $i = 1, 2$. Without loss of generality, one can set (see Fig. 1)

$$b = \frac{R_{10}}{R_{20}} > 1. \quad (2)$$

When the volume of the system remains constant during fusion, for aggregate $i = 1, 2$, one has

$$\rho_i \equiv \rho(\theta_i) \equiv \frac{R_i(\theta_i)}{R_{i0}} = 2^{2/3} (1 + \cos \theta_i)^{-2/3} (2 - \cos \theta_i)^{-1/3}. \quad (3)$$

Thus, the dynamics of the fusion process is completely determined by the time dependence of the fusion angles $\theta_1(t)$ and $\theta_2(t)$, which are related through eqn (1). The values of these two angles change from $\theta_1(0) = \theta_2(0) = 0$ to $\theta_1(\infty) = \theta_{\max}$ and

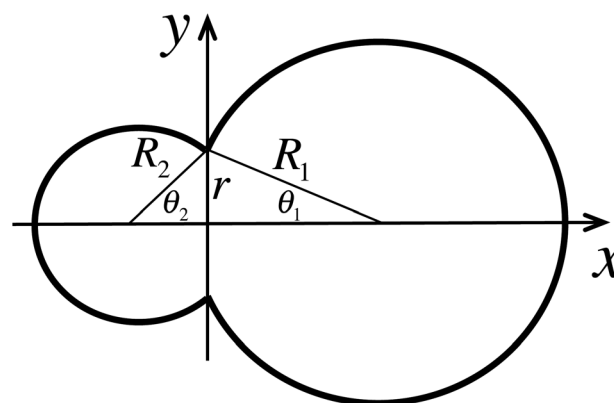


Fig. 1 Axial cross section of two uneven fusing aggregates. At any given time, the shape of the system (two contiguous spherical caps) is characterized by the geometrical parameters: R_1 , R_2 , θ_1 and θ_2 , out of which only three are independent.

$\theta_2(\infty) = \pi - \theta_{\max}$. According to eqn (3) and (2), the angle $\theta_{\max} < \pi/2$, and it obeys the equation

$$\rho(\theta_{\max}) = (1 + b^{-3})^{1/3} \quad (4)$$

Similarly to the fusion of even aggregates, the time dependence $\theta_i(t)$, $i = 1, 2$, can be determined from energy conservation. Because of the slow flow within the highly viscous fusing aggregates, the rate of decrease of the surface energy, dW_s/dt , can be equated to the rate, dW_η/dt , at which energy is dissipated due to viscosity,^{16,36} i.e.,

$$\frac{dW_s}{dt} = \gamma \frac{dS}{dt} = \frac{dW_\eta}{dt} = -2\eta \int_V \left(\frac{\partial v_n}{\partial x_m} \right)^2 dV, \quad (5)$$

where γ , η and S are respectively the surface tension coefficient, viscosity and surface area of the system, $v_{nm} \equiv \partial v_n / \partial x_m$, with $n, m \in \{x, y, z\}$, is the strain rate tensor, and summation over repeated indices is implied.

By defining

$$f_i \equiv f(\theta_i) = \rho(\theta_i) \frac{1 + \cos \theta_i}{2}, \quad i = 1, 2, \quad (6)$$

the surface area of the system can be written as

$$S = S_1 + S_2 = S_{10}f_1 + S_{20}f_2, \quad (7)$$

where $S_{i0} = 4\pi R_{i0}^2$ is the initial surface area of the i^{th} , $i = 1, 2$, spherical aggregate.

Next, assuming a uniform biaxial extensional flow in both spherical caps during the fusion process, the corresponding strain rate tensors are diagonal and (in the coordinate system of Fig. 1) can be written^{15,35,36}

$$v_{nm}^{(i)} = \text{diag}[u_i, -u_i/2, -u_i/2], \quad u_i = \partial v_x^{(i)} / \partial x. \quad (8)$$

In agreement with volume conservation, the flow field obeys the continuity equation $\nabla \cdot \mathbf{v}^{(i)} = \text{Tr}\{v_{nm}^{(i)}\} = 0$, $i = 1, 2$. Thus, $[v_{nm}^{(i)}]^2 = 3u_i^2/2$, and, taking into account volume conservation, $V_i = V_{i0} = S_{i0}R_{i0}/3$, eqn (5) becomes

$$\gamma(S_{10}f_1\dot{\theta}_1 + S_{20}f_2\dot{\theta}_2) = -\eta(u_1^2S_{10}R_{10} + u_2^2S_{20}R_{20}), \quad (9)$$

where the dot on a symbol represents time derivative and $f_i = df(\theta_i)/d\theta_i$. Next, we make the approximation^{15,16,36}

$$u_i \approx -\frac{v_x^{(i)}}{R_i} \approx -\frac{1}{R_i} \frac{d(R_i \cos \theta_i)}{dt} \equiv g_i \dot{\theta}_i, \quad (10)$$

where

$$g_i \equiv g(\theta_i) = \frac{1}{\rho(\theta_i)} \frac{d[\rho(\theta_i) \cos \theta_i]}{d\theta_i}, \quad i = 1, 2. \quad (11)$$

Finally, inserting eqn (10) and (11) into eqn (9), after some algebra, one obtains an equation that can be used to numerically determine the time dependence of the fusion angle θ_1 as a function of time

$$I_1 \equiv I(\theta_1) = - \int_0^{\theta_1} \frac{b^2 g_1^2 + b^{-1} g_2^2 h^2}{b^2 f_1' + f_2' h} d\theta_1 = \frac{t}{\tau}, \quad (12)$$

where $h \equiv h(\theta_1) = d\theta_2/d\theta_1$, with θ_2 expressed as a function of θ_1 from eqn (1), and b is given by eqn (2). We define the characteristic fusion time^{15,16,34} as

$$\tau = \eta R_{10} / \gamma. \quad (13)$$

According to eqn (12), similarly to even aggregates, the fusion angle θ_1 (and, implicitly, θ_2) is only a function of t/τ and does not depend explicitly on the size of the system, albeit it does depend on the dimensionless (asymmetry) parameter $b = R_{10}/R_{20}$. The radius R_{10} appears only in the expression of the fusion time (13).

From eqn (12) one can recover the result for the fusion of even spherical aggregates by setting $R_{10} = R_{20} \equiv R_0$, $b = 1$, $h = 1$, and by removing the indices 1 and 2; one obtains

$$- \int_0^\theta \frac{g^2(\varphi)}{f'(\varphi)} d\varphi = 2 \int_0^\theta \rho(\varphi) \tan \varphi d\varphi = \frac{t}{\tau}, \quad (14)$$

with $\tau = \eta R_0 / \gamma$. A simple and accurate analytical approximation to eqn (14) can be found by setting $\rho(\varphi) \approx 1$; the result is $\cos \theta \approx \exp(-t/2\tau)$, which leads to the previously obtained expression^{15,16}

$$(r/R)^2 = \sin^2 \theta \approx 1 - \exp(-t/\tau). \quad (15)$$

If the volume of the fusing aggregates changes in time (e.g., decreases), eqn (12) needs to be corrected to account for this change. Let us assume that the decrease of the radii (i.e. the linear size) of the two ($i = 1, 2$) spherical aggregates, kept apart to avoid fusion, is governed by the time dependent dimensionless quantity $a(t)$, such that $R_{i0}(t) = a(t)R_{i0}(0)$. In the experiments reported below the function $a(t)$ can be well approximated by the expression

$$a(t) = a_0 + (1 - a_0) \exp(-\lambda t), \quad (16)$$

where $a_0 = a(\infty) \leq 1$ is the relative change of the linear dimension of the system during its complete volume relaxation, and λ is the rate of this process. This change in volume (which has biological origin) will affect the fusion process of the aggregates. While the geometry of the fusing aggregates will remain the same as in the constant volume case (i.e., two contiguous spherical caps) the linear size of the system will change in time by a factor $a(t)$. In addition, the time dependence of the fusion angles $\theta_{1,2}(t)$ will also be affected. An approximate equation for $\theta_1(t)$ can be derived from eqn (9) by replacing R_{i0} and S_{i0} with $a(t)R_{i0}$ and $a^2(t)S_{i0}$, respectively. Then, following the derivation of eqn (12) one arrives at

$$I(\theta_1) = \frac{1}{\tau} \int_0^t \frac{dr'}{a(r')}. \quad (17)$$

For $a(t)$ given by eqn (16), the integral on the right hand side in eqn (17) can be calculated analytically with the result

$$I(\theta_1) = \frac{\ln[1 + a_0(\exp(\lambda t) - 1)]}{\tau \lambda a_0}. \quad (18)$$

Thus, $\theta_1(t)$ [determined by solving numerically eqn (17) or (18)] depends parametrically on $b = R_{10}/R_{20}$, τ , a_0 and λ . The corresponding result for the constant volume case [*i.e.*, eqn (12)] is recovered by setting $a_0 = 1$ in the above equations.

Finally, it is convenient to define the functions $q(t) = \sin^2 \theta_i(t)$, for $\theta_i(t)$ determined from the non-volume-conserving eqn (17) and (18), and $q_0(t) = \sin^2 \theta_i(t)$, for $\theta_i(t)$ determined from the volume-conserving eqn (12). To further simplify notations, for uneven aggregates we have omitted the fusion angle index $i = 1, 2$ in the newly defined quantities q and q_0 . A comparison of eqn (17) and (12) suggests that when the volume of the system decreases during fusion (*i.e.*, $a(t) < 1$, as observed in our experiments) $q(t/\tau)$ could be well approximated with the volume conserving result, $q_0(t/\tau_{\text{eff}})$, albeit with a smaller effective characteristic fusion time, $\tau_{\text{eff}} = c_a \tau < \tau$, (see also Section 3), *i.e.*,

$$q(t/\tau) \approx q_0(t/c_a \tau), 0 < a_0 < c_a < 1. \quad (19)$$

This result implies that a decrease in the system's volume accelerates the fusion process.

2.2. CPD simulation

CPD is an effective computational method for describing and predicting the time evolution of passive biomechanical relaxation processes of multi-cellular aggregates. A typical such relaxation process is the fusion of spheroidal bioink particles during post bioprinting structure formation. The CPD method was described in great detail elsewhere.^{15,16} To make the paper self-contained, below we provide a brief summary of the method.

In the CPD formalism, individual cells are coarse grained into a finite number, N_{CP} , of equal volume regions, described by *cellular particles* (CPs). CPs interact *via* short-range contact forces with both an attractive (*i.e.*, adhesive) and a repulsive (*i.e.*, excluded volume) component. In addition, within a cell CPs are held together by a confining potential that maintains the integrity of the cell, and thus acts as an effective cell membrane. The dynamics of CPs is described by an overdamped Langevin equation. The time evolution of a multicellular system (in particular the variation of its shape) is determined by calculating and recording the trajectories of all CPs.

Quantitatively, the equation of motion for the i^{th} CP, ($i = 1, \dots, N_{\text{CP}}$), in cell n , ($n = 1, \dots, N$), is the Langevin equation³⁷

$$\mu \frac{d\mathbf{r}_{i,n}}{dt} = \mathbf{F}_{1,i,n} + \mathbf{F}_{2,i,n} + \mathbf{f}_{i,n}(t), \quad (20)$$

where $\mathbf{r}_{i,n}$ is the position vector of the CP, μ is the friction coefficient, $\mathbf{F}_{1,i,n}$ is the force due to intracellular interactions, exerted by CPs inside the n^{th} cell, and $\mathbf{F}_{2,i,n}$ is the force due to intercellular interactions, exerted by CPs from the other cells. The random force, $\mathbf{f}_{i,n}(t)$, is due to the stochastic environment inside the cell that ultimately leads to cell surface fluctuations that play an important role in cell motility.^{38,39} $\mathbf{f}_{i,n}(t)$ is modeled as a Gaussian white noise with zero mean and variance $\langle \mathbf{f}_{i,n,\alpha}(t) \mathbf{f}_{j,m,\beta}(0) \rangle = 2D\mu^2 \delta(t) \delta_{ij} \delta_{nm} \delta_{\alpha\beta}$, with α and β representing vector

component indices, and D characterizing the strength of the intracellular force fluctuations.^{15,16}

The deterministic forces in eqn (20) can be expressed in terms of the intracellular, V_1 , and intercellular, V_2 , pairwise CPD potential energies as

$$\mathbf{F}_{1,i,n} = - \sum_{\substack{j=1 \\ j \neq i}}^{N_{\text{CP}}} \partial V_1(|\mathbf{r}_{i,n} - \mathbf{r}_{j,n}|) / \partial \mathbf{r}_{i,n}, \quad (21a)$$

$$\mathbf{F}_{2,i,n} = - \sum_{\substack{m=1 \\ m \neq n}}^N \sum_{j=1}^{N_{\text{CP}}} \partial V_2(|\mathbf{r}_{i,n} - \mathbf{r}_{j,m}|) / \partial \mathbf{r}_{i,n}, \quad (21b)$$

where

$$V_1(r) = V_{\text{LJ}}(r; \varepsilon_1, \sigma_1, 0) + H(r - \alpha) \cdot \frac{k}{2} (r - \alpha)^2, \quad (22a)$$

$$V_2(r) = V_{\text{LJ}}(r; \varepsilon_2, \sigma_2, \delta), r < r_c, \quad (22b)$$

with

$$V_{\text{LJ}}(r; \varepsilon, \sigma, \delta) = 4\varepsilon \left[\left(\frac{\sigma}{r + \delta} \right)^{12} - \left(\frac{\sigma}{r + \delta} \right)^6 \right] \quad (22c)$$

a modified Lennard-Jones (LJ) potential, and $H(r)$ the Heaviside step function. In eqn (22a), $\sigma \equiv \sigma_1$ determines the linear size of a CP and ε_1 quantifies the strength of the interaction between CPs within a cell. For $r > \alpha$, where $\alpha \approx \sigma_1 N_{\text{CP}}^{1/3}$ determines the linear size of a cell, the second (quadratic) term in $V_1(r)$ represents an *elastic confining potential* characterized by the elastic constant k . In the expression of $V_2(r)$, the short cut-off distance, $r_c \approx 1.5\sigma_1$, guarantees that only CPs located at the contact surface between contiguous cells contribute to their adhesive interaction, whose strength is controlled by ε_2 . The shift parameter $\delta = 2^{1/6}(\sigma_2 - \sigma_1)$ makes the minimum of $V_2(r)$ coincide with that of $V_1(r)$ at $r_0 = 2^{1/6}\sigma_1$.

It is convenient to define the following CPD length, time and energy units

$$\mathcal{L} = \sigma, \quad \mathcal{T} = \frac{\sigma^2}{D}, \quad \varepsilon = E_T = \mu D, \quad (23)$$

where E_T is referred to as the “biological fluctuation energy”.⁴⁰ In these units all CPD model parameters are dimensionless, pure numbers. In particular, $\sigma = D = \mu = 1$. The other CPD model parameters (in CPD units) are determined such that the simulated multicellular system behaves as a complex liquid, and the shape of two fusing spherical aggregates in the CPD simulation matches, as closely as possible, the one observed experimentally, *i.e.*, two attached spherical caps.^{15,16} For $N_{\text{CP}} = 10$, these values, determined from a large number of CPD simulations,¹⁵ are as follows: $\alpha = 2 \approx N_{\text{CP}}^{1/3}$, $k = 10$, $\varepsilon_1 = 1.48$, $\varepsilon_2 = 40$, $\sigma_2 = 5$, $\delta = 4.5$, and $r_c = 1.5$.

In all our CPD simulations, the numerical integration of the equations of motion, eqn (20), for CPs was performed using a Langevin dynamics integrator implemented in the freely available massively parallel molecular dynamics package LAMMPS,⁴¹ with an integration time step $\Delta t = 10^{-4}$.

2.3. Experimental

Here we summarize the experimental procedures used in this work.

Materials. Human skin fibroblasts (HSFs) were purchased from the American Type Culture Collection (CRL-2522; ATCC, Manassas, VA). Dulbecco's Modified Eagle Medium (DMEM), Phosphate Buffered Saline (PBS), F12 Nutrient Mixture (Ham's), Sodium Pyruvate and Penicillin/Streptomycin were purchased from Gibco®, Life Technologies (Green Island, New York), HyClone Fetal Bovine Serum (FBS) was purchased from Thermo Fisher (Waltham, Massachusetts). Gelatin (porcine skin gelatin) was obtained from Sigma (St. Louis, MO).

Cell culture. Human skin fibroblasts, were cultured in DMEM with Ham's F12, 20% FBS, antibiotics (penicillin/streptomycin and gentamicin), glutamine 2 mM, sodium pyruvate 0.1 M, on gelatin coated dishes and were maintained at 37 °C in a humidified atmosphere containing 5% CO₂. In each subculture, the cells were washed twice with PBS and detached using a 0.1% Trypsin EDTA solution.

Aggregate preparation. Spherical cell aggregates were prepared using a recently in-house developed device, the "Egg Holder Aggregate Maker" (EHAM), which is similar to the device used in ref. 42. For this device, small wells, 1 mm in diameter and depth were created in an agarose mold using special plastic templates. The wells were positioned in a hexagonal pattern (hence EHAM). Cells were trypsinized and removed from Petri dishes and centrifuged in 15 ml tubes for 5 min at 2000 rpm. Subsequently, the cells were counted and remixed with medium at different concentrations. In this experiment the cell solutions of 4, 8 and 16 million cells per milliliter of medium have been used to have different size of aggregates. The cell solutions were pipetted over the holes in agarose mold as quickly as possible and were incubated for 48 hours. During this time cells settled down in the holes, and formed spherical cell aggregates.

Fusion experiments. Every cell aggregate was observed under the microscope and combination of the same size and different size aggregates were selected to start the fusion experiment. 24-well plate culture dishes were used and each well was covered with 3 droplets of agarose to prevent the sticking of aggregates to the plastic. Wells were filled with medium. Even and uneven pairs of aggregates were placed carefully contiguously, using a hair loop, in each single well. The fusion process was recorded over a week by taking snapshots at different time periods with a Nikon camera (Japan) attached to an Olympus IX70 (Center Valley, PA) inverted microscope. Images were analyzed using *Mathematica*.⁴³

3. Results and discussion

To test the continuum theory presented in Section 2.1, we have studied the fusion of both even and uneven spherical aggregates using both CPD simulations and experiments with HSF aggregates. In each case, snapshots of the fusing aggregates were taken throughout the fusion process. For a snapshot taken at time t , the corresponding fusion angles $\theta_{1,2}(t)$ and radii $R_{1,2}(t)$ were determined by fitting the contour of the fusing aggregates

with that of the axial cross section of two contiguous spherical caps (*i.e.*, two touching circular arcs), as shown in Fig. 1.

Next, the characteristic fusion time τ [see eqn (13)], and the volume change parameters a_0 and λ [see eqn (16)], were determined by fitting $\sin^2 \theta_{1,2}$ vs. $\Delta t = t - t_0$ from the snapshots to $q(\Delta t/\tau)$ or $q_0(\Delta t/\tau)$, functions defined at the end of Section 2.1. Here, t_0 is an "initial time" fitting parameter that accounts for our inability (in both CPD simulations and experiments) to determine precisely the initial time when fusion started (*i.e.*, when the two spherical aggregates touch at a single point). Before calculating τ , we have determined the change in volume of the system during fusion by fitting $R_i(t)$ vs. $\Delta t = t - t_0$ from the snapshots with

$$R_i(t) = R_{i,0}a(t)\rho[\theta_i(t)], \quad i = 1, 2. \quad (24)$$

We have found that the volume of the system is conserved in CPD simulations (*i.e.*, $a_0 = 1$), and it decreased, according to eqn (16), in the fusion experiments with HSF aggregates. Furthermore, this procedure provided good starting values for the parameters a_0 , λ_0 and t_0 , which were then refined in the more involved fitting procedure for determining τ .

Next, we present exemplary results for the fusion of both even and uneven aggregates from both CPD simulations and experiments.

3.1. CPD simulation

In all CPD simulations, the spherical aggregates were pre-equilibrated and (in order to initiate the fusion process) placed within an initial distance σ (*i.e.*, the size of one CP). The values of the CPD model and simulation parameters (in CPD units) are listed at the end of Section 2.2. The CPD simulations of the fusion of even (uneven) aggregates were performed on 32 (24) CPUs of a dual core 2.8 GHz Intel Xeon EM64T cluster with a performance of around $8 \times 10^3 \mathcal{T} \text{ day}^{-1}$ ($2.5 \times 10^3 \mathcal{T} \text{ day}^{-1}$). The entire fusion process of even (uneven) aggregates took about $3 \times 10^3 \mathcal{T}$ ($5 \times 10^3 \mathcal{T}$).

Even aggregates. Each of the two identical spherical aggregates contained $N = 500$ cells and had an initial radius $R_0 = 10.2$. Several representative snapshots of the fusion process are shown in Fig. 2a. In all snapshots the shape of the fusing aggregates is that of two connected spherical caps (*cf.* Fig. 1). Indeed, in each case the solid contour, representing the theoretical prediction of Section 2.1, matches very well the shape of the fusing aggregates. By rendering in different colors the CPs in the cells from the two initial aggregates (Fig. 2a), we can see from the snapshots that, in agreement with previous findings, during fusion there is almost no mixing between the cells from different aggregates.

The $\sin^2 \theta$ vs. $\Delta t = t - t_0$ dependence from the CPD simulation is shown in Fig. 2b as open circles. The data can be well fitted to the theoretical prediction $q_0(\Delta t/\tau)$ [*cf.* eqn (15)] with $\tau = 640$ and $t_0 = -190$. The negative initial time, t_0 , indicates that by the time the first usable snapshots are taken the fusion process is already underway, characterized by a fusion angle $\theta > 0$.

The inset to Fig. 2b shows that the volume of the system does not change during the CPD simulation. Indeed, the simulation data for $R(t)/R_0$ (open circles) lies along the theoretical prediction, eqn (24), with $a(t) = a_0 = 1$.

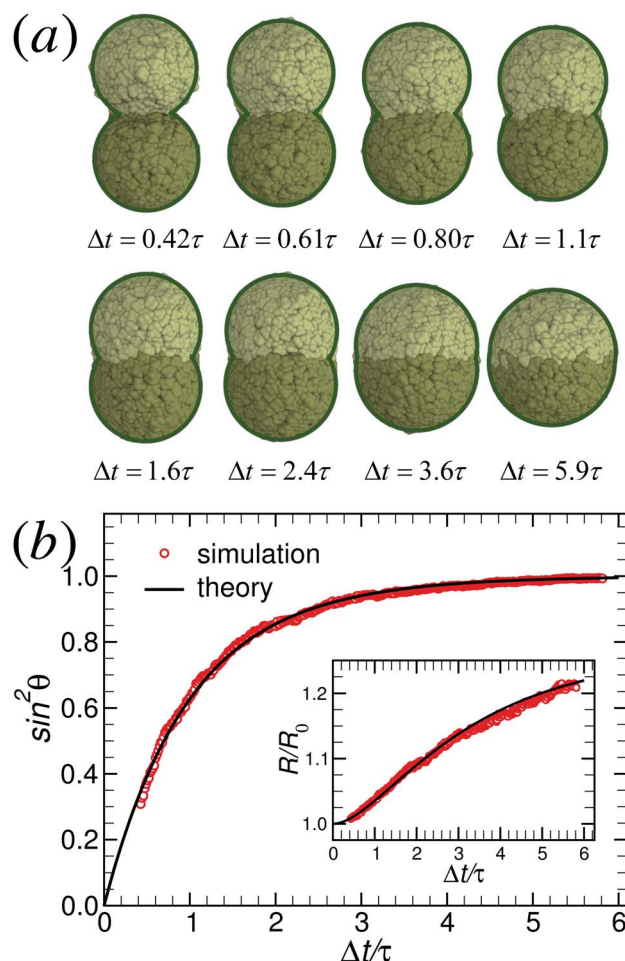


Fig. 2 (a) Snapshots from the CPD simulation of the fusion of two even aggregates. The solid-line contours represent the theoretical shapes of the fusing aggregates. (b) Theoretical fit (solid curve) to the CPD simulation data (open circles) for $\sin^2 \theta$ vs. $\Delta t = t - t_0$, corresponding to $\tau = 640$ and $t_0 = -190$ in CPD time units. Inset: time dependence of $R(t)/R_0$.

Uneven aggregates. The two uneven aggregates consisted of $N_1 = 2000$ and $N_2 = 400$ cells, respectively. The corresponding initial radii were $R_{10} = 15.9$ and $R_{20} = 9.4$, with $b = R_{10}/R_{20} = 1.7$. Representative snapshots of the fusing aggregates are shown in Fig. 3a. In this case too, the theoretical prediction (solid contour lines) for the shape of the fusing aggregates (*i.e.*, two uneven contiguous spherical caps; see Fig. 1) is remarkably accurate. Also, there is (almost) no mixing between the cells from different aggregates.

The time dependence of $\sin^2 \theta_{1,2}$ from the CPD simulation, shown as open circles in Fig. 3b, can be well fitted with $q_0(\Delta t/\tau)$ [cf. eqn (12)] for $\tau = 1121$ and $t_0 = -190$. As in all our CPD simulations, the volume of the system remained constant throughout the fusion process.

3.2. Experiment

All fusion experiments were performed with EHAM aggregates as described in Section 2.3.

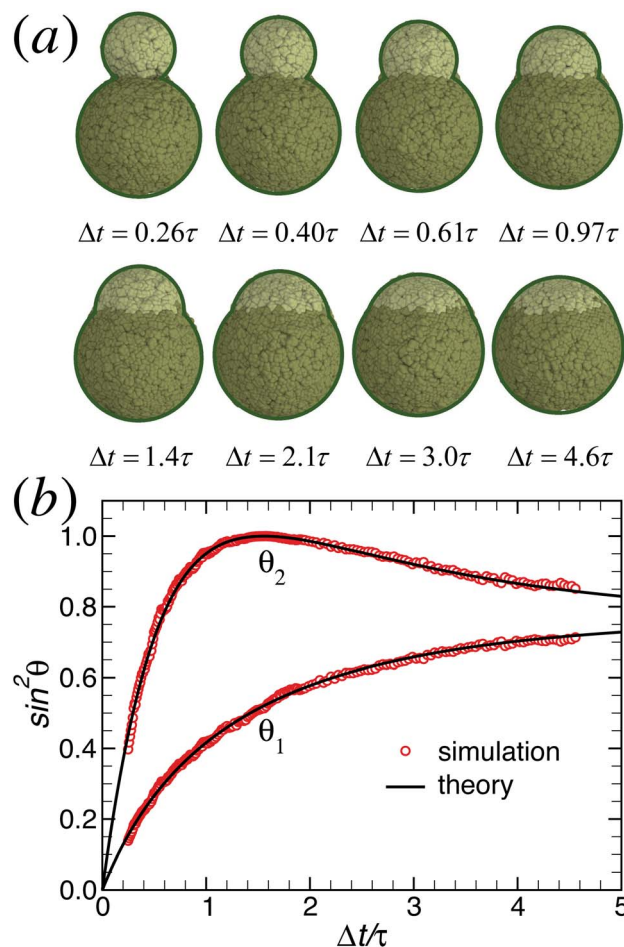


Fig. 3 (a) Snapshots from the CPD simulation of the fusion of two uneven aggregates, with $N_1 = 2000$, $N_2 = 400$ and $b = R_{10}/R_{20} = 1.7$. The solid-line contours represent the theoretical shapes of the fusing aggregates. (b) Theoretical fit (solid curve) to the CPD simulation data (open circles) for $\sin^2 \theta_{1,2}$ vs. $\Delta t = t - t_0$, corresponding to $\tau = 1121$ and $t_0 = -190$ in CPD time units.

Even aggregates. Snapshots taken during the fusion of two identical HSF aggregates, with initial radius $R_0 = 274 \mu\text{m}$, are shown in Fig. 4a. Similarly to the CPD simulations and previous experimental results, the shape of the fusing HSF aggregates indeed is that of two connected spherical caps (*cf.* Fig. 1). The $\sin^2 \theta$ vs. $\Delta t = t - t_0$ dependence, shown in Fig. 4b as open circles, can be well fitted with $q(\Delta t/\tau)$ [cf. eqn (18)] (solid curve in Fig. 4b), which accounts for volume change during fusion, with $\tau = 48.0 \text{ h}$, $t_0 = 9.3 \text{ h}$, $a_0 = 0.73$ and $\lambda^{-1} = 50 \text{ h}$. Note that the characteristic fusion time τ and the volume relaxation time λ^{-1} are almost the same. In spite of this fact, and of the noticeable decrease in the volume of the system (*i.e.*, $V(\infty)/V(t_0) = a_0^3 \approx 0.4$), the difference between the theoretical fits $q(\Delta t/\tau)$ (solid curve in Fig. 4b) and $q_0(\Delta t/\tau)$ (dashed curve in Fig. 4b) is relatively small. In fact, in agreement with eqn (19), $q(\Delta t/\tau)$ is almost indistinguishable from $q_0(\Delta t/c_a\tau)$ (dashed-dotted curve in Fig. 4b), where $c_a = (1 + a_0)/2 = 0.87$. Based on this result, one may conclude that, in general, experimental fusion data for cell aggregates with decreasing system volume can be analyzed (and

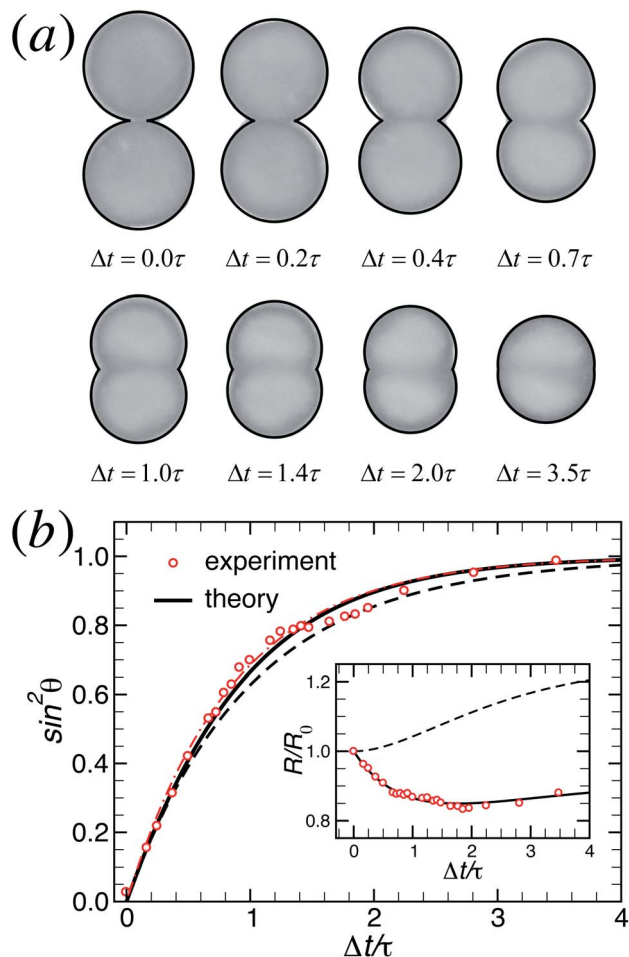


Fig. 4 (a) Snapshots from the fusion of two even HSF aggregates with $R_0 = 274 \mu\text{m}$. The solid-line contours represent the theoretical shapes of the fusing aggregates. (b) Theoretical fit (solid curve) to the experimental data (open circles) for $\sin^2 \theta$ vs. $\Delta t = t - t_0$, corresponding to $\tau = 48.0$ and $t_0 = 9.3$ hours. The dashed (dot-dashed) curve represents the volume conserving theoretical result with same (effective) characteristic fusion time τ (0.865τ). Inset: time dependence of $R(t)/R_0 = a(t)\rho[\theta(t)]$. The solid curve corresponds to $a_0 = 0.73$ and $\lambda^{-1} = 50$ hours. The strong deviation from the volume conserving dashed curve indicates a substantial decrease in volume during fusion.

predicted) quantitatively using the constant volume result provided that τ is replaced by a smaller effective fusion time $\tau_{\text{eff}} = c_a \tau < \tau$.

The inset to Fig. 4b shows that indeed the radius of the fusing spherical caps changes in time according to eqn (24), with $a(t)$ given by eqn (16). The deviation from the volume conserving (*i.e.*, $a(t) = a_0 = 1$) case (dashed curve) is evident.

Uneven aggregates. Snapshots taken during the fusion of two uneven HSF aggregates, characterized by $b = R_{10}/R_{20} = 1.7$ and initial radii $R_{10} = 302 \mu\text{m}$ and $R_{20} = 178 \mu\text{m}$, are shown in Fig. 5a. As expected, the overall shape of the fusing aggregates can be well fitted with two uneven contiguous spherical caps (*c.f.* Fig. 1). Again, the $\sin^2 \theta_{1,2}$ vs. $\Delta t = t - t_0$ dependence, shown in Fig. 5b as open circles, is accurately reproduced by $q(\Delta t/\tau)$ [*c.f.* eqn (18)] for the fitting parameters: $\tau = 48.9$ h, $t_0 = -3.0$ h, $a_0 = 0.67$ and $\lambda^{-1} = 52.6$ h (solid curves in Fig. 5b). Similarly to

the fusion of even aggregates: (i) the difference between the theoretical fits $q(\Delta t/\tau)$, corresponding to volume change with $a_0 = 0.67$ (solid curves in Fig. 5b), and $q_0(\Delta t/\tau)$, corresponding to constant volume (dashed curves in Fig. 5b) is relatively small; and (ii) $q_0(\Delta t/c_a \tau)$ (dashed-dotted curve in Fig. 5b), with $c_a = 0.87$, approximates well $q(\Delta t/\tau)$.

The fact that we have obtained practically the same values for the volume change parameter, $a_0 \approx 0.7$, and the volume relaxation rate, $\lambda \approx 0.02 \text{ h}^{-1}$, in both fusion experiments (involving even and uneven HSF aggregates), suggests that the time dependence of the volume relaxation of a multicellular system depends primarily on the used cell type (HSF in our case) and the employed preparation method. This point is illustrated in Fig. 6, where the relative change in system size, $R_s(t)/R_s(0) = [V(t)/V(0)]^{1/3} = a(t)$, is shown for the described fusion experiments and CPD simulations. Here one defines the system size $R_s(t)$ as the radius of the sphere that would accommodate the entire system at the given time t .

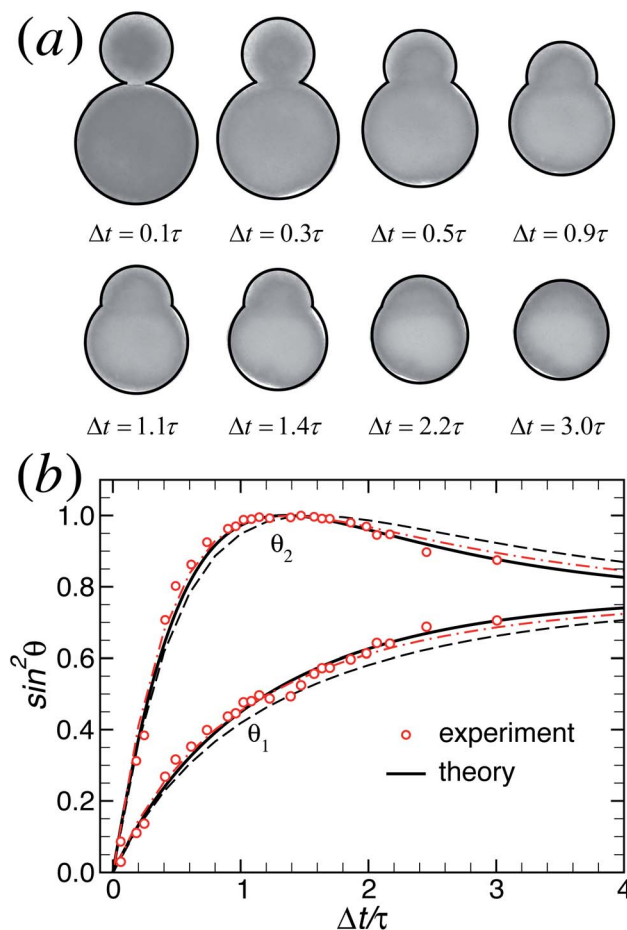


Fig. 5 (a) Snapshots from the fusion of two uneven HSF aggregates, characterized by $b = R_{10}/R_{20} = 1.7$, and $R_{10} = 302 \mu\text{m}$. The solid-line contours represent the theoretical shapes of the fusing aggregates. (b) Theoretical fit (solid curve) to the experimental data (open circles) for $\sin^2 \theta_{1,2}$ vs. $\Delta t = t - t_0$, corresponding to $\tau = 48.9$ and $t_0 = -3.0$ hours. The dashed (dot-dashed) curve represents the volume conserving theoretical result with the same (effective) characteristic fusion time τ (0.865τ).

Furthermore, according to Fig. 6, the volume of the multicellular system does not change during CPD simulations. Finally, one should mention that the values of the parameters a_0 and λ can also be determined by following the volume relaxation of a single spherical aggregate.

3.3. CPD simulations predict the outcome of the fusion of multicellular aggregates

As shown in the previous section $\sin^2 \theta_{1,2}(t)$ for the fusion of HSF aggregates, during which the volume of the system decreases, can be accurately approximated with the theoretical result, $q_0(\Delta t/\tau_{\text{eff}})$ that assumes volume conservation, albeit with a smaller effective characteristic fusion time $\tau_{\text{eff}} = c_a \tau$ [cf. eqn (19)]. Thus, based on the above results, one may conclude that it is possible to predict the outcome of the fusion of multicellular aggregates (or, in principle, any shape relaxation process that involves multicellular systems), accompanied by change in volume, by employing directly the corresponding CPD simulations, during which the volume of the system is conserved. Indeed, here we propose and demonstrate such a direct approach (that does not require the application of the intermediate continuum theory) by making use of the fusion experiments and CPD simulations presented above. For convenience, we refer to the fusion experiments (CPD simulations) of the even and uneven aggregates as E1 and E2 (S1 and S2), respectively. Furthermore, we refer to E1 and S1 as “calibration” experiment and CPD simulation.

First, one fits $q_{\text{E1}}(\Delta t) = \sin^2 \theta(\Delta t)$ from E1 (Section 3.2) directly with $q_{\text{S1}}(\Delta t/\mathcal{T}_1)$ as obtained from S1 (Section 3.1). The procedure is shown in Fig. 7b. As a result, one obtains the CPD time unit $\mathcal{T}_1 = 3.9$ min and the time shift between S1 and E1, $\Delta t_1 = -21.6$ h (a fitting parameter defined through $\Delta t = t - \Delta t_1$). Once \mathcal{T}_1 has been determined, one can use the fusion angle from S1, $\theta_{\text{S1}}(\Delta t/\mathcal{T}_1)$, to construct the contours of the fusing

aggregates at any desired time Δt . Several representative fusion snapshots from E1 are shown in Fig. 7a. The dashed curves represent the contours of the constant volume fusing aggregates in S1. However, if one corrects the radius of the fusing aggregates in S1 through eqn (24) and (16), with the predetermined $a_0 = 0.7$ and $\lambda = 0.02 \text{ h}^{-1}$, one obtains the solid contours in Fig. 7a that match the results from E1.

Next, in order to predict E2 directly from S2, one needs to determine the CPD time unit \mathcal{T}_2 in terms of \mathcal{T}_1 and the initial radii of the fusing aggregates in E1, S1, E2 and S2. To this end, we recall that $q_{\text{E1}}(\Delta t) \approx q(\Delta t/\tau_{\text{E1}}) \approx q_0(\Delta t/c_a \tau_{\text{E1}})$ (see Section 3.2), and similarly $q_{\text{S1}}(\Delta t/\mathcal{T}_1) \approx q_0(\Delta t/\tau_{\text{S1}} \mathcal{T}_1)$. Thus, from $q_{\text{E1}}(\Delta t) \approx q_{\text{S1}}(\Delta t/\mathcal{T}_1)$ follows that

$$c_a \tau_{\text{E1}} \approx \tau_{\text{S1}} \mathcal{T}_1. \quad (25)$$

Using the same reasoning for E2 and S2, one obtains a similar equation

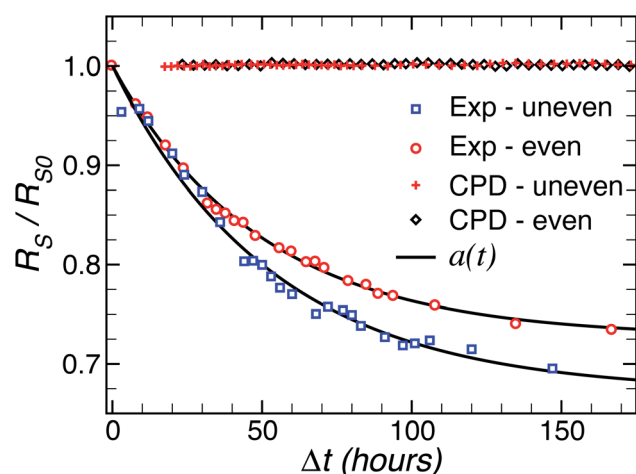


Fig. 6 Change in volume of the system during the fusion process characterized by the quantity $R_s(t)/R_s(0) = [V(t)/V(0)]^{1/3} = a(t)$. In CPD simulations the volume is conserved, while during the fusion of HSF aggregates the volume decreases according to eqn (16) (solid curves). For the considered fusion of even (uneven) aggregates: $a_0 = 0.73$ ($a_0 = 0.67$) and $\lambda = 0.020$ ($\lambda = 0.019$) hours^{-1} .

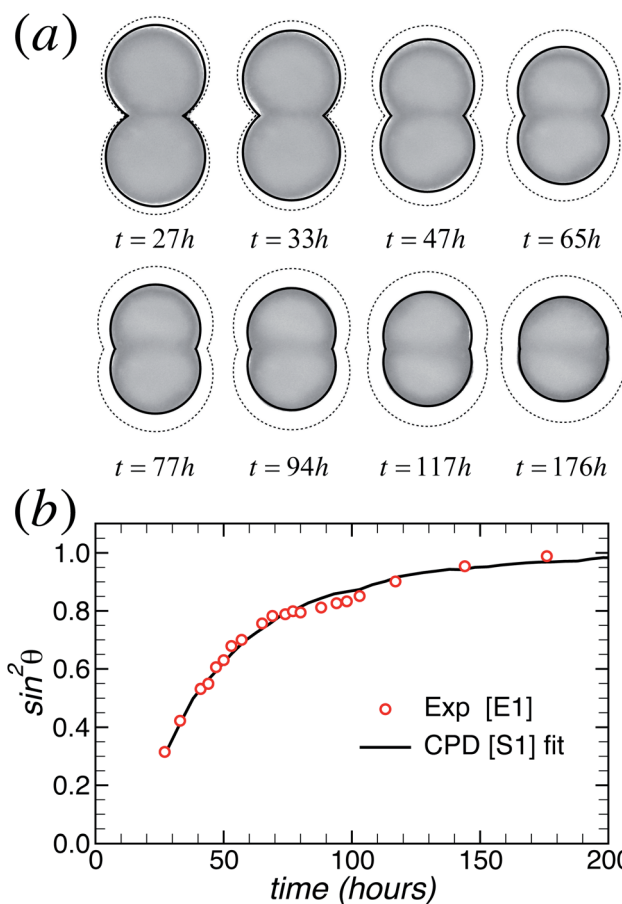


Fig. 7 (a) Snapshots from the fusion of two identical HSF aggregates with $R_0 = 274 \mu\text{m}$. The solid (dashed) contour represents the shape of the fusing aggregates as determined from the CPD simulation, with (without) change in volume taken into account (as explained in the text). (b) Fit of the $\sin^2 \theta$ vs. $\Delta t = t - \Delta t_1$ dependence as obtained from the experimental E1 data (open circles) in (a) with the corresponding CPD simulation S1 data (solid curve). The fit provides the CPD time unit and the time shift between the S1 and E1 data respectively as $\mathcal{T}_1 = 3.9$ min and $\Delta t_1 = -21.6$ h.

$$c_a \tau_{E2} \approx \tau_{S2} \mathcal{T}_2, \quad (26)$$

where the parameter c_a has (approximately) the same value as in eqn (25). From these two equations one can determine the \mathcal{T}_2 CPD time unit as

$$\mathcal{T}_2 \equiv \mathcal{T}_{2,\tau} \approx \mathcal{T}_1 \frac{\tau_{E2} \tau_{S1}}{\tau_{E1} \tau_{S2}}. \quad (27)$$

Finally, using eqn (13) and assuming that the combination of the material constants η/γ for E1 (S1) has the same value as for E2 (S2), one arrives at an expression for \mathcal{T}_2 that does not require any direct input from the theoretical analysis of Section 2.1

$$\mathcal{T}_2 \equiv \mathcal{T}_{2,R} \approx \mathcal{T}_1 \frac{R_{10,E2} R_{0,S1}}{R_{0,E1} R_{10,S2}}. \quad (28)$$

With the data from Section 3.2, one obtains $\mathcal{T}_{2,\tau} = 2.3$ min and $\mathcal{T}_{2,R} = 2.7$ min. The relatively small (<15%) difference

between these two CPD time units stems from the about 10% deviation of $\eta/\gamma = \tau/R_{10}$ between S1 and S2 and E1 and E2.

The time dependence of $q_{E2}(\Delta t)$ as predicted through $q_{S2}(\Delta t/\mathcal{T}_2)$ is shown in Fig. 8b. The solid (dashed) curve corresponds to $\mathcal{T}_{2,R}$ ($\mathcal{T}_{2,\tau}$). While the use of $\mathcal{T}_{2,\tau}$ instead of $\mathcal{T}_{2,R}$ provides a visibly better prediction for $q_{E2}(\Delta t)$, it is important to emphasize that both \mathcal{T}_2 values provide the same contour of the fusing aggregates, as shown in Fig. 8a. Again, by employing eqn (24) to correct the size of the system due to the decrease in volume, one obtains excellent prediction for the conformational change of the fusing aggregates in E2 by using S2. It should be emphasized that, by using eqn (28) for \mathcal{T}_2 , the prediction of E2 from the CPD simulations S2 and S1, and the “calibration” experiment E1, does not make any use of the intermediate continuum theory (Section 2.1). Thus, the proposed method should be applicable for predicting the experimental outcome of any shape relaxation process of a multicellular system from the corresponding CPD simulation. This is an important practical result because, in general, there is no theoretical continuum model that describes the shape relaxation of a multicellular system of arbitrary shape.

4. Conclusion

In this and previous publications^{15,16} we have demonstrated that *cellular particle dynamics* is an effective computational method for describing and predicting the shape evolution of multicellular systems during biomechanical relaxation, *e.g.*, the fusion of discrete bioink particles. As such, CPD is most useful for predicting the outcome of postprinting structure formation following 3D bioprinting. In the present work we have extended the CPD formalism in several important ways.

First, we have shown that volume conserving CPD simulations can in fact describe the fusion of multicellular aggregates whose volume decreases significantly during the fusion process (Section 2.1). To this end, we have studied both experimentally (using HSF aggregates) and through CPD simulations the fusion of both even and uneven spherical aggregates. To establish the connection between the corresponding CPD and experimental results, we have extended the intermediary continuum theory to the fusion of uneven aggregates for both constant and variable volume systems. With this new theory, we have shown that, by employing an effective (reduced) fusion time, the constant and variable volume results practically coincide. This finding implies that using loose bioink units, whose volume decreases during post-printing fusion, may significantly accelerate the formation of the desired continuous biological structure. Another advantage of using loose aggregates is that these may be less prone to form necrotic cores throughout the bioprinting process.

Second, we have proposed and demonstrated a two-step approach for directly connecting CPD simulations to corresponding experiments without the need of using the intermediate continuum theory (Section 3.3). In the first step the CPD time unit \mathcal{T}_1 is determined by fitting the results of a “calibration” experiment (E1) with the results from the

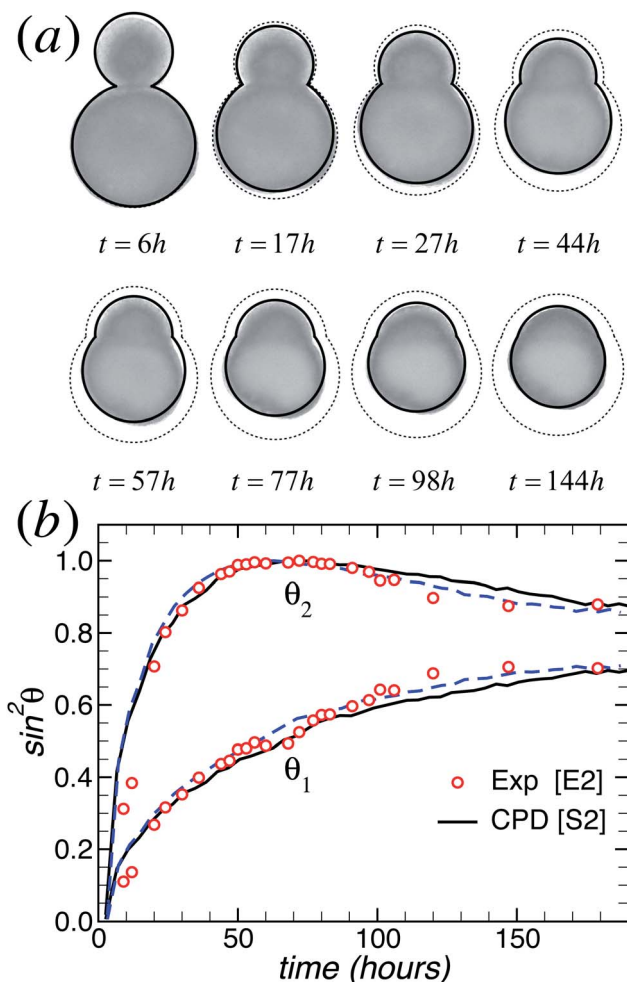


Fig. 8 (a) Snapshots from the fusion of two uneven HSF aggregates with $R_{10}/R_{20} = 1.7$ and $R_{10} = 302 \mu\text{m}$. The solid (dashed) contour represents the predicted shape of the fusing aggregates obtained from CPD simulation S2 when the change in volume is (not) taken into account. (b) CPD simulation S2 prediction of $\sin^2 \theta_{1,2}$ vs. $\Delta t = t - \Delta t_2$ for the E2 fusion experiment of the uneven HSF aggregates (open circles). Solid [dashed] curve corresponds to CPD time unit \mathcal{T}_2 given by eqn (28) [eqn (27)].

corresponding CPD simulation (S1). Next, one determines the CPD time unit \mathcal{T}_2 for the CPD simulation (S2) corresponding to the “target” fusion experiment (E2). Once \mathcal{T}_2 is known, E2 is predicted from S2. Besides the relative initial sizes of the experimental (E1 and E2) and CPD (S1 and S2) systems, \mathcal{T}_2 also depends on the corresponding relative change of the material quantity η/γ [cf. eqn (27) and (28)]. When the sizes of the calibration and target systems are (almost) equal, as in the case considered in Section 3.3, the contribution from η/γ can be neglected and \mathcal{T}_2 can be determined from eqn (28). However, our preliminary studies show that there is a noticeable system size dependence of η/γ in both CPD simulations and experiments that may need to be taken into account [through eqn (27)] for a more accurate evaluation of \mathcal{T}_2 (and, implicitly, a more accurate prediction of the target experiment). We plan to report on the system size dependence of η/γ in a forthcoming publication.

Acknowledgements

The authors benefited from useful discussions on some of the experimental details with Karoly Jakab. This work was supported by a grant from the National Science Foundation (PHY-0957914). Computational resources were generously provided by the University of Missouri Bioinformatics Consortium.

References

- 1 C. J. Ferris, K. G. Gilmore, G. G. Wallace and M. In het Panhuis, *Appl. Microbiol. Biotechnol.*, 2013, **97**, 4243–4258.
- 2 S. Tasoglu and U. Demirci, *Trends Biotechnol.*, 2013, **31**, 10–19.
- 3 U. Demirci and G. Montesano, *Lab Chip*, 2007, **7**, 1139–1145.
- 4 S. Moon, S. K. Hasan, Y. S. Song, F. Xu, H. O. Keles, F. Manzur, S. Mikkilineni, J. W. Hong, J. Nagatomi, E. Haeggstrom, A. Khademhosseini and U. Demirci, *Tissue Eng.*, 2010, **16**, 157–166.
- 5 K. Jakab, C. Norotte, B. Damon, F. Marga, A. Neagu, C. L. Besch-Williford, A. Kachurin, K. H. Church, H. Park, V. Mironov, R. R. Markwald, G. Vunjak-Novakovic and G. Forgacs, *Tissue Eng., Part A*, 2008, **14**, 413–421.
- 6 C. Norotte, F. S. Marga, L. E. Niklason and G. Forgacs, *Biomaterials*, 2009, **30**, 5910–5917.
- 7 C. M. Smith, A. L. Stone, R. L. Parkhill, R. L. Stewart, M. W. Simpkins, A. M. Kachurin, W. L. Warren and S. K. Williams, *Tissue Eng.*, 2004, **10**, 1566–1576.
- 8 C. M. Smith, J. J. Christian, W. L. Warren and S. K. Williams, *Tissue Eng.*, 2007, **13**, 373–383.
- 9 X. Cui, T. Boland, D. D. D’Lima and M. K. Lotz, *Recent Pat. Drug Delivery Formulation*, 2012, **6**, 149–155.
- 10 F. Guillemot, A. Souquet, S. Catros, B. Guillotin, J. Lopez, M. Faucon, B. Pippenger, R. Bareille, M. Remy, S. Bellance, P. Chabassier, J. C. Fricain and J. Amedee, *Acta Biomater.*, 2010, **6**, 2494–2500.
- 11 L. Koch, M. Gruene, C. Unger and B. Chichkov, *Curr. Pharm. Biotechnol.*, 2013, **14**, 91–97.
- 12 Y. Fang, J. P. Frampton, S. Raghavan, R. Sabahi-Kaviani, G. Luker, C. X. Deng and S. Takayama, *Tissue Eng.*, 2012, **18**, 647–657.
- 13 K. Jakab, C. Norotte, F. Marga, K. Murphy, G. Vunjak-Novakovic and G. Forgacs, *Biofabrication*, 2010, **2**, 1.
- 14 F. Marga, K. Jakab, C. Khatiwala, B. Shepherd, S. Dorfman, B. Hubbard, S. Colbert and F. Gabor, *Biofabrication*, 2012, **4**, 022001.
- 15 I. Kosztin, G. Vunjak-Novakovic and G. Forgacs, *Rev. Mod. Phys.*, 2012, **84**, 1791–1805.
- 16 E. Flenner, L. Janosi, B. Barz, A. Neagu, G. Forgacs and I. Kosztin, *Phys. Rev. E: Stat., Nonlinear, Soft Matter Phys.*, 2012, **85**, 031907.
- 17 E. Flenner, F. Marga, A. Neagu, I. Kosztin and G. Forgacs, *Curr. Top. Dev. Biol.*, 2008, **81**, 461–483.
- 18 G. M. Odell, G. Oster, P. Alberch and B. Burnside, *Dev. Biol.*, 1981, **85**, 446–462.
- 19 F. Graner and J. A. Glazier, *Phys. Rev. Lett.*, 1992, **69**, 2013–2016.
- 20 J. A. Glazier and F. Graner, *Phys. Rev. E: Stat. Phys., Plasmas, Fluids, Relat. Interdiscip. Top.*, 1993, **47**, 2128–2154.
- 21 E. Palsson and H. G. Othmer, *Proc. Natl. Acad. Sci. U. S. A.*, 2000, **97**, 10448–10453.
- 22 D. Drasdo and G. Forgacs, *Dev. Dyn.*, 2000, **219**, 182–191.
- 23 G. W. Brodland, *J. Biomech. Eng.*, 2002, **124**, 188–197.
- 24 G. W. Brodland, *Appl. Mech. Rev.*, 2004, **57**, 47–76.
- 25 M. S. Hutson, G. W. Brodland, J. Yang and D. Viens, *Phys. Rev. Lett.*, 2008, **101**, 148105.
- 26 Y. Sun and Q. Wang, *Soft Matter*, 2013, **9**, 2172–2186.
- 27 T. J. Newman, *Mathematical Biosciences and Engineering*, 2005, **2**, 611–624.
- 28 S. A. Sandersius and T. J. Newman, *Phys. Biol.*, 2008, **5**, 15002.
- 29 T. J. Newman, *Curr. Top. Dev. Biol.*, 2008, **81**, 157–182.
- 30 S. A. Sandersius, C. J. Weijer and T. J. Newman, *Phys. Biol.*, 2011, **8**, 045007.
- 31 S. A. Sandersius, M. Chuai, C. J. Weijer and T. J. Newman, *Phys. Biol.*, 2011, **8**, 045008.
- 32 G. Forgacs and S. Newman, *Biological physics of the developing embryo*, Cambridge University Press, 2005.
- 33 K. Jakab, B. Damon, F. Marga, O. Doaga, V. Mironov, I. Kosztin, R. Markwald and G. Forgacs, *Dev. Dyn.*, 2008, **237**, 2438–2449.
- 34 J. Frenkel, *J. Phys.*, 1945, **9**, 385–391.
- 35 J. D. Eshelby, *Trans. Am. Inst. Min., Metall. Pet. Eng.*, 1949, **185**, 806.
- 36 C. T. Bellehumeur, M. Kontopoulou and J. Vlachopoulos, *Rheol. Acta*, 1998, **37**, 270–278.
- 37 P. M. Chaikin and T. C. Lubensky, *Principles of condensed matter physics*, Cambridge University Press, Cambridge, New York, NY, USA, 1995, p. 699.
- 38 R. Gordon, N. S. Goel, M. S. Steinberg and L. L. Wiseman, *J. Theor. Biol.*, 1972, **37**, 43–73.
- 39 J. C. M. Mombach, J. A. Glazier, R. C. Raphael and M. Zajac, *Phys. Rev. Lett.*, 1995, **75**, 2244–2247.

- 40 D. A. Beysens, G. Forgacs and J. A. Glazier, *Proc. Natl. Acad. Sci. U. S. A.*, 2000, **97**, 9467–9471.
- 41 S. Plimpton, *J. Comput. Phys.*, 1995, **117**, 1–19.
- 42 N. Tejavibulya, J. Youssef, B. Bao, T.-M. Ferruccio and J. R. Morgan, *Biofabrication*, 2011, **3**, 034110.
- 43 Wolfram Research, Inc, Mathematica, Version 8.0, Champaign, IL, 2010.